

Entropic lattice Boltzmann model for surface tension effects on liquid plug rupture in two- and three-dimensional channels

Yingying Hu ^{1,*}, F. Romanò ², and James B. Grotberg³¹*School of Low-Carbon and Power Engineering, China University of Mining and Technology, Xuzhou, Jiangsu 221116, China*²*University of Lille, CNRS, ONERA, Arts et Métiers Institute of Technology, Centrale Lille, UMR 9014-LMFL-Laboratoire de Mécanique des Fluides de Lille-Kampé de Fériet, F-59000 Lille, France*³*Department of Biomedical Engineering, The University of Michigan, Ann Arbor, Michigan 48109, USA*

(Received 16 March 2023; accepted 15 June 2023; published 13 July 2023)

We established an entropic lattice Boltzmann model to study surface tension effects on quasiequilibrium liquid plug rupture in two- and three-dimensional channels. The surface tension coefficient is supposed to be an increasing function of plug-gas density ratios, and the contact angle is not uniquely determined by surface tension. The influence of the surface tension coefficient on plug rupture is combined with the effects of viscosity and inertia. The plug is more likely to rupture at a greater Ohnesorge number (the ratio of viscous forces and the geometric mean of surface tension and inertial forces), which positively correlates to the plug's surface area-to-volume ratio and negatively to channel thickness. With the increasing of the initial plug length (at the fixed density ratio and surface tension), four patterns of plug rupture are observed in three-dimensional channels, four holes, two holes, one hole, and no hole (i.e., no rupture). There exists minimum initial plug length for a certain rupture pattern to appear. The four-hole rupture happens only in thick channels (the aspect ratio of channel thickness to width between 0.6 and 1.0). No two-hole rupture is available in square channels. Plug rupture in two-dimensional channels is similar to that in the three-dimensional, but simpler without the definition of the channel thickness and the four-hole rupture. The minimum plug lengths indicating two-dimensional rupture patterns quadratically decrease with the contact angle and slightly increase with surface tension. The results indicate not only the entropic lattice Boltzmann method's great potential in the study of multiphase fluid flows but also a clinical implication that increasing wetting ability of mucus plugs might be an effective practice in lung airway reopening. A final successful solution, however, depends on full understanding of all factors, especially the forces of surface tension, viscosity, and inertia.

DOI: [10.1103/PhysRevFluids.8.073603](https://doi.org/10.1103/PhysRevFluids.8.073603)

I. INTRODUCTION

Mucus plug rupture is of great interest in the study of lung airway closure and reopening, a popular topic basically related to mucociliary clearance and epithelial cell damage [1–6]. The challenges of studying the problem lie in not only mucus properties but also mucus-airway structure. Lung airway mucus is a complex hydrogel mixed with proteins, salts, lipids, and water, and its properties are still a fruitful and active research topic [7]. Current dynamic studies usually simplify mucus properties as Newtonian [2,8], or more accurately, non-Newtonian with given shear-strain relations, for example, shear-thinning/thickening, viscoplastic, and elastoviscoplastic [1,3,5,9–12].

*Corresponding author: hyy@cumt.edu.cn

In mucus plug formation, viscoelasticity contributes to a second peak of wall shear stress, related to elastic instability and equally severe as the first one due to Newtonian stresses [8,12]. Plug rupture is favored as mucus is shearing-thinning, but hindered by the mucus yield stress [1,3].

Lung walls are coated by two liquid layers, serum and mucus. The two fluid interfaces from the lung wall to the airway lumen, serum-mucus and mucus-air, introduce another significant factor, surface tension, into the mucus dynamic study. Though models for both layers have been available [2], the single layer of mucus is currently more concerned [5]. At small scales such as lower airways with dimensions of millimeter, surface tension plays important roles in mucus dynamics [1,2,5]. Surface tension-induced Plateau-Rayleigh instability is a major reason for mucus plugs to form [2]. Reduced surface tension by surfactant also reduces stress and damage upon epithelial cells as a mucus plug propagates in lung airways [13,14].

In the study of mucus plug dynamics, numerical computation, as a power tool in research, is extensively used. A main effort is to solve mucus-air interface deformation and rupture, at which numerical methods of interface tracking and capture are available: marker and cell, volume of fluid, level set, immersed boundary, to name but a few [2,15–17]. For the Navier-Stokes equations-based computational fluid dynamics (CFD), interface formulations of these methods are often arduous and complicated.

The lattice Boltzmann method (LBM), directly solving the Boltzmann equation instead of the Navier-Stokes equations, is an alternative to the conventional CFD, and burgeoning in numerical studies of fluid dynamics. Particularly in the study of multiphase fluid flows, the LBM has inherent rationales of physics by taking surface tension as an interaction force at a more foundational level of kinetic molecular dynamics [18–22]. There are generally four LB models for multiphase flows, pseudopotential [23,24], mean-field free-energy [25–27], lattice gas-based color gradient [28–30], and a hybrid of LBM and conventional CFD [31,32]. Each multiphase LB model has its own advantages and disadvantages. The pseudopotential model, completely based on kinetic theory, is relatively simple and versatile, and has been the most widely used multiphase LB model [20,24,29]. The later three, with a continuum quantity for interfaces between immiscible fluids, are phenomenological [20,29].

The LBM still faces challenges. Fluid flows at high Mach numbers are difficult to simulate [18]. The LBM is some problematic with thermodynamic consistency and Galilean invariance [33–36]. Numerical instability may arise when the Reynolds number is high, spatial gradients of flow become too large, and the distribution function turns negative [18,37,38]. Boundary condition modeling is indirect, since the LBM solves a distribution function, rather than physical quantities [18,39]. Poor representation of dynamic quantities on boundaries is another source of instability.

Efforts have been made to improve LBM's numerical stability, for instance, using multiple relaxation times instead of a single relaxation time of the standard LBM [40,41], and introducing regularization or a precollision step prior to the collision step while maintaining simplicity of the Bhatnagar-Gross-Krook operator [38,42,43]. These approaches usually need extra computational time, and/or lack universal criteria on the choice of stable reliable relaxation times [38,42]. Another promising approach that can greatly boost LBM stability is the entropic LBM (ELBM) by introducing Boltzmann's entropy function to improve the nonequilibrium distribution function [28,38,44,45]. Considerable computational cost is also required to solve entropy-related nonlinear equations. Opinions on ELBM efficiency are divided [38,44]. Nonetheless the ELBM is "unconditionally" stable [44]. Boltzmann's entropy function in the context of the classical continuous Boltzmann equation is so far the only kinetic theory that ensures the second-order accuracy of the Navier-Stokes equations after recovering the primitive variables [46].

In this study, we will therefore employ ELBM for unraveling the detailed deformation and rupture of a mucus plug in a small lung airway. Thus, we study mainly surface tension effects on quasiequilibrium mucus plug rupture in two- (2D) and three-dimensional (3D) channels. The pseudopotential approach is used as the multiphase LB model, and the ELBM is employed to improve numerical stability in spite of its computational cost.

II. METHODS

A. Entropic lattice Boltzmann equation

The entropic lattice Boltzmann equation is formulated as [47,48]

$$f_m(\vec{x}_m + \vec{c}_m \delta t, t + \delta t) = f_m(\vec{x}, t) + \alpha \beta [f_m^{\text{eq}}(\rho, \vec{u}) - f_m(\vec{x}, t)] + S_m. \quad (1)$$

We use a three-dimensional 19-speed lattice scheme (i.e., D3Q19),

$$\begin{aligned} c_x &= [0, 1, -1, 0, 0, 0, 0, 1, -1, 1, -1, 1, -1, 1, -1, 0, 0, 0, 0], \\ c_y &= [0, 0, 0, 1, -1, 0, 0, 1, 1, -1, -1, 0, 0, 0, 0, 1, -1, 1, -1], \\ c_z &= [0, 0, 0, 0, 0, 1, -1, 0, 0, 0, 0, 1, 1, -1, -1, 1, 1, -1, -1]. \end{aligned}$$

That is, $m = 0, \dots, b$, and $b = 18$ in Eq. (1). The discrete distribution functions, $f_m(\vec{x}, t)$, provide the probability of finding a particle at the lattice location \vec{x} and time t with the discrete velocity \vec{c}_m . Thus, the density and momentum are constructed,

$$\rho = \sum_{m=0}^b f_m, \quad \rho \vec{u} = \sum_{m=1}^b f_m \vec{c}_m.$$

The discrete local equilibria, $f_m^{\text{eq}}(\rho, \vec{u})$, are chosen as a third-order Mach-number expansion of the continuum Maxwell-Boltzmann distribution [48],

$$f_m^{\text{eq}} = \rho w_m \left[1 + \frac{c_{m\lambda} u_\lambda}{c_s^2} + \frac{u_\lambda u_\phi}{2c_s^4} (c_{m\lambda} c_{m\phi} - c_s^2 \delta_{\lambda\phi}) + \frac{u_\lambda u_\phi u_\gamma}{6c_s^6} c_{m\gamma} (c_{m\lambda} c_{m\phi} - 3c_s^2 \delta_{\lambda\phi}) \right], \quad (2)$$

where $\gamma, \lambda, \phi = x, y, z$, respectively, running on spatial dimensions, and $\delta_{\lambda\phi}$ is the Kronecker delta. The weight factors, w_m , are $w_0 = 1/3$, $w_{1-6} = 1/18$, and $w_{7-18} = 1/36$ [20]. The lattice speed of sound, $c_s = c/\sqrt{3}$, is related to the universal gas constant through $RT = c_s^2$ [49]. Here the lattice speed is $c = \delta x / \delta t = 1$ by taking the lattice size and time step as $\delta x = \delta t = 1$, and therefore $c_s = 1/\sqrt{3}$ (units in lattice are omitted if not specified). The equilibria, f_m^{eq} , also act as the minimizer of the discrete entropy function of Boltzmann, i.e., the H -function [47],

$$H = \sum_{m=0}^b f_m \ln \left(\frac{f_m}{w_m} \right).$$

The parameter product, $\alpha\beta$, indicates a characteristic collision frequency of fluid molecules. The parameter, β ($0 < \beta < 1$), is related to the kinematic viscosity,

$$\nu = \frac{c_s^2 \delta t}{2} \left(\frac{1}{\beta} - 1 \right),$$

where $\beta = \frac{1}{2\tau}$ is expressed in terms of the single relaxation time approximation, τ .

The maximum over-relaxation parameter, α , maintains entropy balance in a relaxation step at each node, and secures compliance with the second law of thermodynamics. It is the nontrivial root of the entropy estimate of the H -function [47],

$$H[f + \alpha(f^{\text{eq}} - f)] = H(f).$$

The H -function is solved after the total force balance is applied,

$$H[f' + \alpha(f^{\text{eq}}(\vec{u} + \delta \vec{u}) - f')] = H(f'), \quad (3)$$

in which $f' = f + [f^{\text{eq}}(\bar{u} + \delta\bar{u}) - f^{\text{eq}}(\bar{u})]$. The velocity difference, $\delta\bar{u}$, is defined by using the force, \vec{F} ,

$$\delta\bar{u} = \frac{\vec{F}}{\rho}\delta t.$$

We use the Newton-Raphson method to find α . Equation (1) is reduced to the standard LB equation (with single τ) as $\alpha = 2$ [48].

The source terms, S_m , are calculated using the exact difference approach [20,50],

$$S_m = f_m^{\text{eq}}(\rho, \bar{u} + \delta\bar{u}) - f_m^{\text{eq}}(\rho, \bar{u}). \quad (4)$$

B. Forces

The total force, \vec{F} , usually includes the interaction force within the fluid, \vec{F}_f , the interaction force between the fluid and solid, \vec{F}_s , and the gravitational force, $\vec{F}_g = \rho\vec{g}$,

$$\vec{F} = \vec{F}_f + \vec{F}_s + \vec{F}_g.$$

The former two, \vec{F}_f and \vec{F}_s , are calculated using the pseudopotential multiphase LB scheme [20,47,48],

$$\vec{F}_f(\vec{x}, t) = -G\psi(\vec{x}, t) \sum_{m=0}^b w_m \psi(\vec{x} + \vec{c}_m \delta t, t) \vec{c}_m, \quad (5)$$

$$\vec{F}_s(\vec{x}, t) = \psi_w(\vec{x}, t) \sum_{m=0}^b w_m s(\vec{x} + \vec{c}_m \delta t, t) \vec{c}_m. \quad (6)$$

In the above equations, the coupling constant, G , indicates interaction strength of the fluid. The indicator functions, $s(\vec{x} + \vec{c}_m \delta t)$, equal to 1 for solid nodes and 0 otherwise [47]. The function, $\psi(\vec{x}, t)$, is generalized density (i.e., effective mass), and $\psi_w(\vec{x}_{\text{wall}}) = k_w \psi(\vec{x}_{\text{fluid}})$ at wall. The parameter k_w , positive and varying in the neighborhood of 1.0, is adjustable to simulate fluid-solid surface interaction. Approximately, $k_w > 1.0$ denotes a wetting (hydrophilic) liquid at wall and $k_w < 1.0$ nonwetting (hydrophobic) [48].

C. Peng-Robinson equation of state

We use the Peng-Robinson equation of state [51],

$$p = \frac{\rho R_g T}{1 - b\rho} - \frac{a\Xi\rho^2}{1 + 2b\rho - b^2\rho^2}, \quad (7)$$

in which p is thermodynamic pressure, $a = 0.45724R_g^2 T_c^2 / p_c$, $b = 0.0778R_g T_c / p_c$, $R_g = 1.0$, $\zeta = 0.344$, and $\sqrt{\Xi} = 1 + (0.37464 + 1.54226\zeta - 0.26992\zeta^2)(1 - \sqrt{T/T_c})$ [52]. Suitable for both liquid and gas states, the Peng-Robinson state equation allows a density ratio up to $\mathcal{O}(10^3)$ in multiphase fluid flow. Large pressure or density gradients may indicate liquid-gas interfaces, whose thickness can be as thin as the size about five lattice grids in the current study. We take $a = 0.005$ and $b = 0.0952$ [48]. Thus, $T_c = \frac{0.0778a}{0.45724bR_g} = 0.0729$. According to the Maxwell construction [20], we select three density ratios of liquid and gas, $\chi_\rho = \rho_l / \rho_g = 6.36/0.424 = 15.0$, $7.29/0.181 = 40.2$, and $7.90/0.0784 = 100.7$, at which $T/T_c = 0.870$, 0.792 , and 0.724 , respectively.

The generalized density, ψ , in the force expression (5) is written as the function of pressure and density,

$$\psi = \sqrt{\frac{2(p - c_s^2 \rho)}{c_s^2 G}} \quad \left(\text{i.e., } p = c_s^2 \rho + \frac{1}{2} c_s^2 G \psi^2 \right).$$

The coupling constant, G , is calculated through $G = \text{sgn}(p - c_s^2 \rho)$, a sign function ensuring mathematical applicability of ψ [48,52,53].

D. Boundary and initial conditions

Periodic conditions are extension of the streaming process. We use i, j, k ($i = 0, \dots, i_0, j = 0, \dots, j_0$, and $k = 0, \dots, k_0$) to indicate the integer coordinates of a lattice in the x, y, z -coordinate system. The periodic conditions at $i = 0$ and $i = i_0$ are written as

$$i = 0: \begin{cases} f_{1,0,j,k} = f_{1,i_0,j,k} \\ f_{7,0,j,k} = f_{7,i_0,j-1,k} \\ f_{9,0,j,k} = f_{9,i_0,j+1,k} \\ f_{11,0,j,k} = f_{11,i_0,j,k-1} \\ f_{13,0,j,k} = f_{13,i_0,j,k+1} \end{cases}, \quad i = i_0: \begin{cases} f_{2,i_0,j,k} = f_{2,0,j,k} \\ f_{8,i_0,j,k} = f_{8,0,j-1,k} \\ f_{10,i_0,j,k} = f_{10,0,j+1,k} \\ f_{12,i_0,j,k} = f_{12,0,j,k-1} \\ f_{14,i_0,j,k} = f_{14,0,j,k+1} \end{cases}$$

Standard direct bounceback is used as no-slip wall conditions [48,54]. Walls set at $k = 0$ and $k = k_0$ yield

$$k = 0: \begin{cases} f_{5,i,j,0} = f_{6,i,j,1} \\ f_{11,i,j,0} = f_{14,i+1,j,1} \\ f_{12,i,j,0} = f_{13,i-1,j,1} \\ f_{15,i,j,0} = f_{18,i,j+1,1} \\ f_{16,i,j,0} = f_{17,i,j-1,1} \end{cases}, \quad k = k_0: \begin{cases} f_{6,i,j,k_0} = f_{5,i,j,k_0-1} \\ f_{14,i,j,k_0} = f_{11,i-1,j,k_0-1} \\ f_{13,i,j,k_0} = f_{12,i+1,j,k_0-1} \\ f_{18,i,j,k_0} = f_{15,i,j-1,k_0-1} \\ f_{17,i,j,k_0} = f_{16,i,j+1,k_0-1} \end{cases}$$

Initially, the liquid and gas are at rest. We use Expression (2) to calculate f^{eq} and let $f = f^{\text{eq}}$ with preset densities of the two fluids. The parameter α is initialized to $\alpha = 2.0$.

E. Surface tension

1. Coefficient of surface tension

We use a spherical liquid droplet in a still gas field to estimate surface tension between the droplet liquid and the surrounding gas. Periodic conditions are applied on all boundaries. For a round liquid droplet in equilibrium, the Young-Laplace law gives

$$\Delta p = \frac{2\gamma}{R},$$

in which Δp is the pressure difference between the inside and outside of the droplet, R the droplet radius, and γ the coefficient of surface tension. Three density ratios, $\chi_\rho = 15.0, 40.2, 100.7$, are used to determine the corresponding surface tension, as shown in Fig. 1. The linear relations of Δp with R^{-1} are curve-fitted as

$$\begin{aligned} \chi_\rho = 15.0: & \quad \Delta p = 0.2317R^{-1} & (R_s^2 = 0.9994), \\ \chi_\rho = 40.2: & \quad \Delta p = 0.4598R^{-1} & (R_s^2 = 0.9996), \\ \chi_\rho = 100.7: & \quad \Delta p = 0.6695R^{-1} & (R_s^2 = 0.9995). \end{aligned}$$

The coefficients of determination, R_s^2 , varying between 0.9994 and 0.9996, indicate good linearity between Δp and R^{-1} . The coefficients of surface tension at the density ratios of $\chi_\rho = 15.0, 40.2, 100.7$ are $\gamma_{15} = 0.1159, \gamma_{40} = 0.2299$, and $\gamma_{100} = 0.3348$, respectively, which increase with χ_ρ , and are used in this study.

2. Contact angle

We use a liquid column centered in an h -by- h cross-sectioned channel in equilibrium to determine the contact angle at a given surface tension. The liquid column length is half of the channel, i.e.,

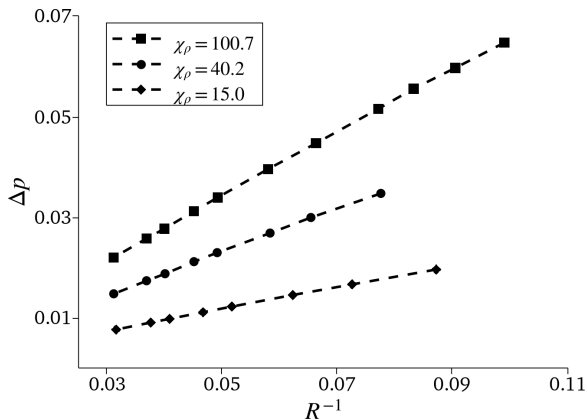


FIG. 1. The pressure difference, Δp , between the inside and outside of the droplet in terms of R^{-1} at the density ratios of $\chi_\rho = 15.0$, 40.2 , and 100.7 .

$8h/2$. The periodic boundary conditions are set at $x = 0, 8h$, and the standard bounceback nonslip wall conditions at $y = 0, h$ and $z = 0, h$.

Figure 2 shows the contact angle, θ , is a function of k_w . The θ_{img} -value (marked by the diamond symbol in Fig. 2) is manually measured from image results using ImageJ, θ_{elbm} (by circle) is calculated through the Young-Laplace law,

$$\Delta p = \frac{2\gamma \cos \theta}{h},$$

and θ_{fit} (by solid line-cross symbol), used in the following study, is the average of the former two.

The good agreements of the results from both the numerical ELBM and the Young-Laplace law shown in Fig. 2, together with Fig. 1, verify the effectiveness of the ELBM proposed in this study [47,55].

E. Parameters of plug rupture

We deal with the forces of surface tension and viscosity in the study, and formulate the plug rupture problem as

$$\text{func}(\rho_l, \rho_g, \nu, \gamma, \theta, l_p, a, h) = 0,$$

where l_p , a , h are initial plug length, channel width, and channel thickness, respectively. The kinematic viscosity here is the same for both the plug and gas, $\nu = 0.133$. It yields five dimensionless parameters,

$$\frac{\rho_l}{\rho_g} (= \chi_\rho), \nu \sqrt{\frac{\rho_l}{l_p \gamma}}, \theta, \frac{l_p}{a}, \frac{h}{a}.$$

The dimensionless parameter, $\nu \sqrt{\frac{\rho_l}{l_p \gamma}}$, is the Ohnesorge number, Oh, indicating the ratio of the viscous force to the geometric mean of the inertial and surface tension forces. The channel thickness is scaled by a , i.e., $H = h/a$. So is the plug length in a 2D channel, $L_p = l_p/a$. For the plug in a 3D channel, we scale its length by Vol/SA (the reciprocal of the ratio of plug surface area, SA, to volume, Vol), instead of a . We also replace l_p with Vol/SA to calculate Oh in 3D. In this study, $a = 100 \sim 1000$ lu (mostly $a = 100$ and 200 lu; lu is the lattice length unit used to distinguish lattice length dimensions from the scaled ones), $L_p = 0.03 \sim 0.185$ (scaled by a here), $\chi_\rho = 15.0, 40.2, 100.7$ as aforementioned, and $\text{Oh} = 0.28 \sim 0.40$. For a mucus plug in the ninth-generation of lung airways, it is estimated $\nu \sim \mathcal{O}(10^{-5})$ m²/s, $\rho_l \sim \mathcal{O}(10^3)$ kg/m³,

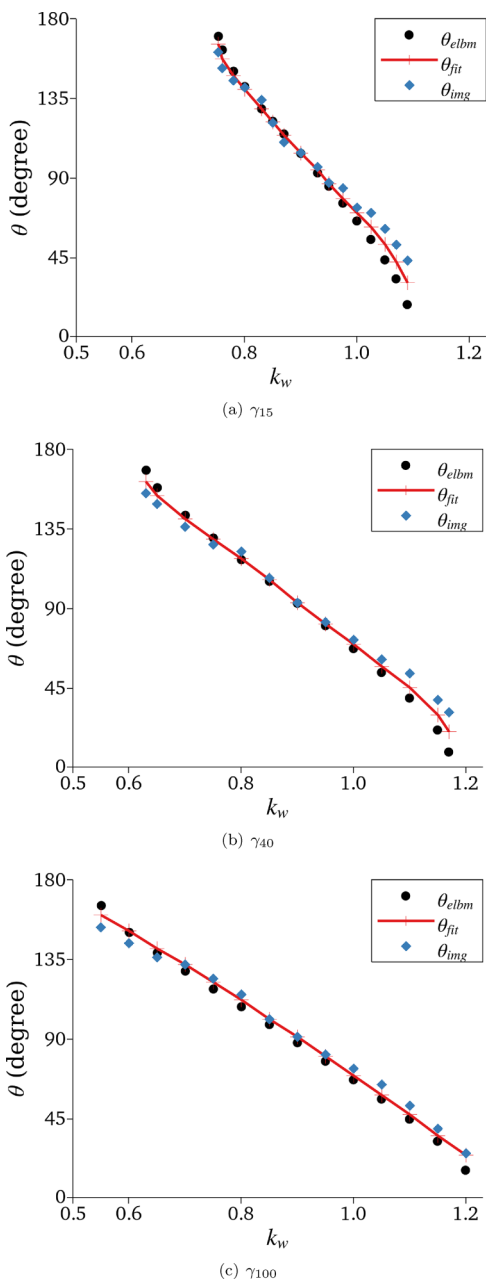


FIG. 2. The contact angle, θ , as a function of k_w at (a) γ_{15} , (b) γ_{40} , and (c) γ_{100} .

$l_p \sim \mathcal{O}(10^{-3})$ mm, and $\gamma \sim \mathcal{O}(10^{-2})$ N/m [3]. So, $Oh \sim \mathcal{O}(10^{-1})$, comparable with the Oh-range in the current study.

III. RESULTS

This study focuses on topological features of plug rupture and the related physics as well. We suppose a cuboidal plug is initially at rest and located in the middle of the L -long channel, as shown

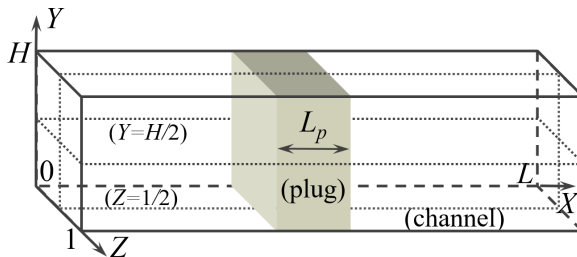


FIG. 3. Geometry of the plug and channel. $Y = H/2$ and $Z = 1/2$: two cross-sections centered in the channel.

in Fig. 3 (where a is used to scale the coordinates, and the dimensions of the channel and the plug). Thus, the process of plug deformation and/or rupture is driven by surface tension only and of quasiequilibrium. In 2D plug rupture, standard bounceback wall conditions are set at $Z = 0, 1$, and periodic conditions at both $X = 0, L$ and $Y = 0, H$ ($0.1 \leq H \leq 1.0$), in which Y -dependent values, for example, H , are physically insignificant. The boundary conditions in 3D plug rupture are similar to those in the 2D above, except that the boundaries $Y = 0, H$ are taken as standard bounceback walls instead of the periodic boundaries in 2D.

A. 2D plug rupture

1. Wetting plugs

Initially a rectangular plug blocks the channel, as shown in Fig. 4(a). The plug is displayed in density contour levels from 0.02 to 7.90 with the color spectrum from the cool of blue to the warm of red (the same with the plug shapes in the following figures). With the initial plug length, L_p , increasing at a given contact angle and given surface tension appear two minimum initial plug lengths, L_{p1} , at which rupture develops from the plug center instead of two central-symmetrical necks of the plug, and L_{p0} ($> L_{p1}$), at which no rupture takes place. Three rupture patterns are observed:

(1) Satellite-droplet-rupture: As $L_p < L_{p1}$, the plug deforms into a spindle attached to L walls, then breaks at the two necks, and finally generates a satellite droplet in the channel middle and two films attached to walls, as shown in Fig. 4(b).

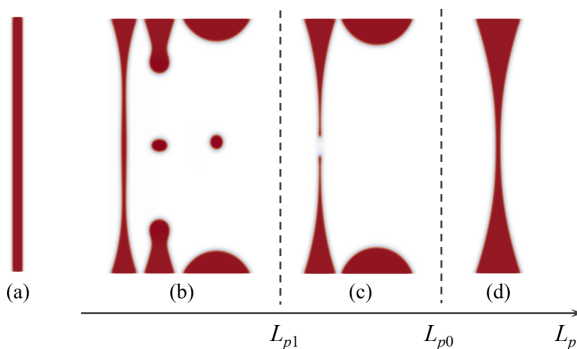


FIG. 4. Plug rupture patterns at $\chi_p = 100.7$, $\gamma_{100} = 0.3348$, and $\theta = 1.20$ rad. (a) A rectangular plug at the initial. (b) Satellite-droplet-rupture: three images of the plug ($L_p = 0.045$) from shortly before and after rupture equilibrium. (c) Film-rupture: two images of the plug ($L_p = 0.05$) shortly after rupture and finally in equilibrium. (d) No-rupture: one image of the plug equilibrium ($L_p = 0.085$).

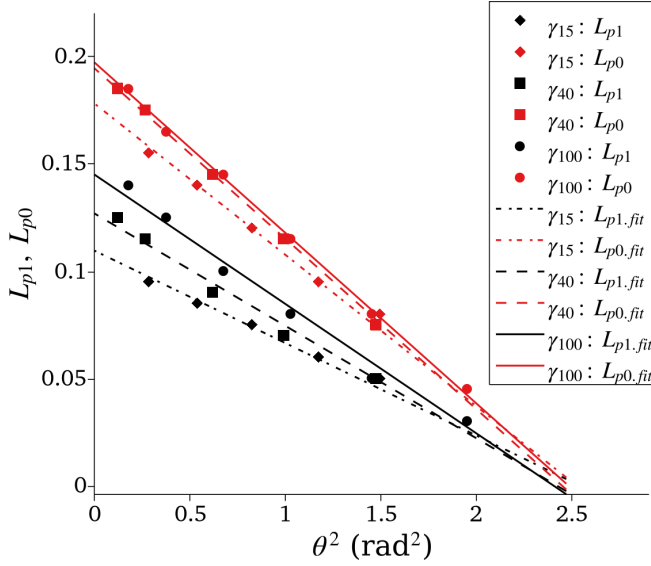


FIG. 5. The minimum initial plug lengths, L_{p1} and L_{p0} , for the possibilities of film-rupture and no-rupture, respectively, in terms of the contact angle, θ^2 , at γ_{15} , γ_{40} , and γ_{100} . (Symbols: the numerical results; lines: the linear curve-fitting results of L_{p1} and L_{p0} in terms of θ^2 with the determination coefficients between 0.9907 and 0.9995.)

(2) Film-rupture: As $L_{p1} \leq L_p < L_{p0}$, rupture starts from the plug center with a single hole (O_1 , without droplet) till two films are attached to walls, as shown in Fig. 4(c).

(2) No-rupture: As $L_p \geq L_{p0}$, there is no rupture, as shown in Fig. 4(d).

Figure 5 shows plug rupture patterns, indicated by L_{p1} and L_{p0} , are decreasing linear functions of the squared contact angle at given surface tension. The smaller contact angle (more wetting) and the larger surface tension, the larger L_{p1} and L_{p0} , say, more likely for the plug to rupture. With the contact angle increasing and the wetting ability of the plug being weakened, both L_{p1} and L_{p0} decline from their maxima at $\theta = 0$ around $0.110 \sim 0.145$ and $0.178 \sim 0.197$, respectively, to zero at the limit of low wetting ability, $\theta = \pi/2$ ($\theta^2 = 2.47 \text{ rad}^2$). The zero-collapsing of L_{p1} and L_{p0} at $\theta = \pi/2$ makes surface tension's effects on plug rupture recognizable only as θ is safely less than $\pi/2$ and the contact angle appear more influential in plug rupture than surface tension as a whole.

2. Nonwetting plugs

Figure 6 shows a nonwetting rectangular plug deforms before and after equilibrium at $L_p = 0.05$, $\chi_\rho = 100.7$, $\gamma_{100} = 0.3348$, and $\theta = 2.46 \text{ rad}$. The plug undergoes a series of amoebic deformation

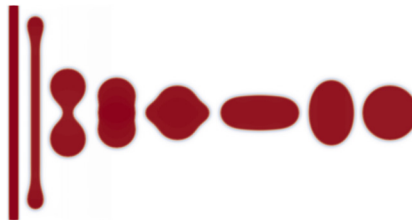


FIG. 6. A nonwetting plug deforms from the initial rectangular shape to the final round droplet in equilibrium. The initial plug is set at $L_p = 0.05$, $\chi_\rho = 100.7$, $\gamma_{100} = 0.3348$, and $\theta = 2.46 \text{ rad}$.

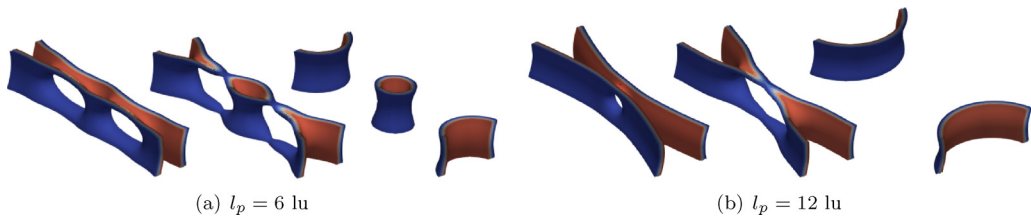


FIG. 7. Two plug rupture patterns, (a) O_2 at $l_p = 6$ lu, and (b) O_2 at $l_p = 12$ lu, in the thin channel, $H = 0.2$.

from a slender-dumbbell shape to a squad dumbbell, a vertical rod, a flying saucer, a horizontal rod, and a football, before becoming round equilibrium. The final round droplet is a self-evidence of surface tension effects of nonwetting liquids.

B. 3D plug rupture

In 3D, wetting plug rupture is studied only at the density ratio, $\chi_\rho = 100.7$, surface tension, $\gamma_{100} = 0.3348$, and contact angle, $\theta = 1.20$ rad.

With one more pair of paralleled walls (at $Y = 0, H$ in Fig. 3) than 2D plug rupture, 3D plugs deform and rupture in more varieties. Based on rupture development at incipience, we define four rupture patterns:

- O_4 : Four holes symmetric about two middle cross-sections, $Y = H/2$ and $Z = 1/2$;
- O_2 : Two holes symmetric about the cross-section, $Z = 1/2$;
- O_1 : One hole co-axial with the channel center line;
- O_0 : No hole, i.e., no rupture.

According to rupture patterns, we specify three types of channels, thin channels as $0 < H \leq 0.4$, moderate as $0.4 < H \leq 0.6$, and thick as $0.6 < H \leq 1.0$. The square channel with $H = 1.0$ is a special thick channel. Figures 7–10 show the plug deformation and rupture in the thin, moderate, thick, and square channels, respectively.

1. Thin channel

Take $H = 0.2$ as an example to show plug rupture in thin channels. Plugs rupture in two patterns (here excluding no rupture, O_0 , and the same in the following without specification), O_2 and O_1 , as shown in Figs. 7(a) and 7(b), respectively. They end up similarly with two plug films attached to the walls, $Z = 0, 1$, except that O_1 has one column left in the middle of the channel [in Fig. 7(a)].

2. Moderate channel

The channel thickness, $H = 0.5$, is used to display plug rupture in moderate channels. Similar to plug rupture in thin channels in Fig. 7, two rupture patterns, O_2 and O_1 , happen. But more deformation configurations appear as larger space is available in the thickness dimension of moderate channels, as shown in Fig. 8. For O_2 -rupture in Fig. 8(a), the plug column in the middle, initially separating the two holes, is long enough so that it later breaks itself from the wall-attached plug mass and a droplet suspends at the center of the channel. But the droplet may disappear when its volume is small. The deformation and rupture of the plug mass attached to walls are similar to 2D plug rupture in Fig. 4, for example, separated round films at walls, though vanishing finally.

3. Thick channel

We use the channel thickness, $H = 0.8$, to study plug rupture in thick channels. With even larger space in the thick dimension, plug rupture displays much richer patterns in thick channels than in the moderate.

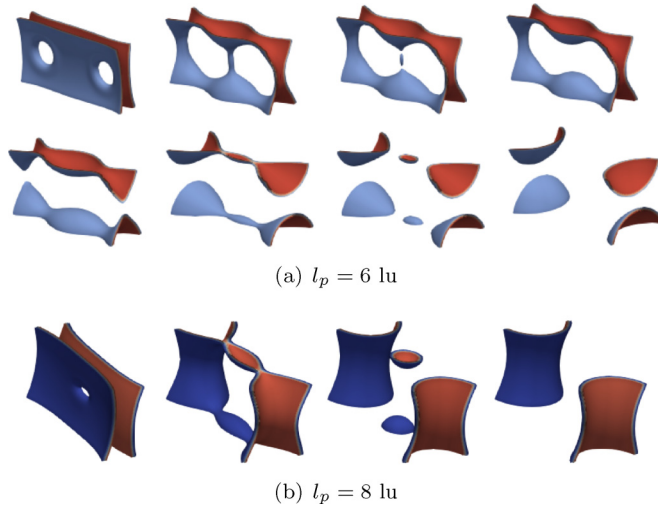


FIG. 8. Two rupture patterns, (a) O_2 at $l_p = 6$ lu, and (b) O_1 at $l_p = 8$ lu, in the moderate channel, $H = 0.5$.

At small initial plug length, Fig. 9(a) shows rupture is initiated with four holes, instead of two in the thin and moderate channels in Figs. 7(a) and 8(a), respectively. Similar to O_2 in Fig. 8(a), however, the plug mass in the thick dimension that separates four holes can also break itself from the surrounding mass and generate a suspending droplet in the middle of the channel, as shown by the top-row images in Fig. 9(a).

Both the O_2 - and O_1 -ruptures are observed in thick channels, too, as initial plug lengths are relatively large, for example, $l_p = 8$ and 12 lu in Figs. 9(b) and 9(c), respectively.

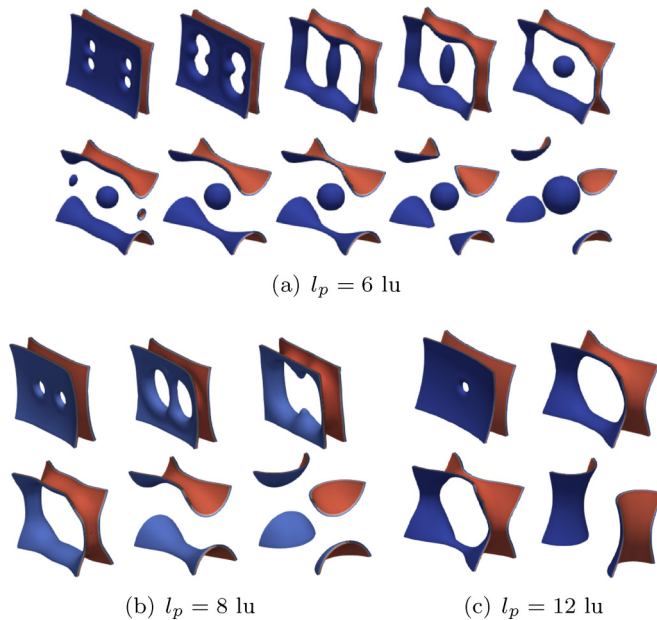
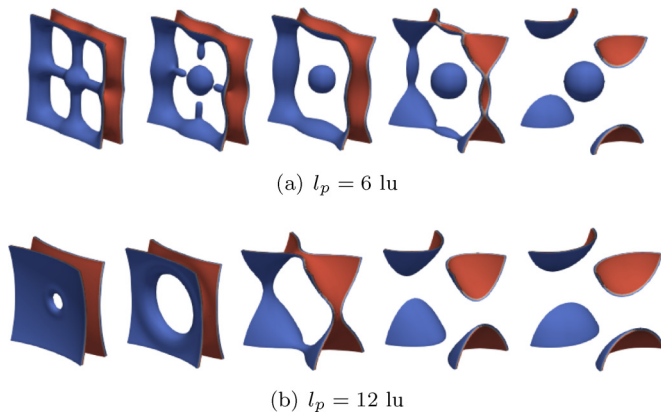


FIG. 9. Three rupture patterns, (a) O_4 at $l_p = 6$ lu, (b) O_2 at $l_p = 8$ lu, and (c) O_1 at $l_p = 12$ lu, in the thick channel, $H = 0.8$.


 FIG. 10. Two rupture patterns, (a) O_4 at $l_p = 6$ lu and (b) O_1 at $l_p = 12$ lu, in the square channel, $H = 1.0$.

4. Square channel

At $H = 1.0$, the square channel renders a rotational symmetry of 90 degrees, i.e., a symmetry order of four, two orders higher than the rectangular but nonsquare channel, and thus is worthy of special concern. Figure 10 shows the plug deforms and ruptures in good 90° -rotational symmetry, which simplifies deformation and rupture configuration of the plug, compared with that in thick nonsquare channels, as shown in Fig. 9 at $H = 0.8$.

As the plug is small, say, $l_p = 6$ lu, the O_4 -rupture appears like that in a generic thick channel in Fig. 9(a). The four holes are also symmetrical about the two diagonals of the square cross section. The holes grow, the plug ribs between two adjacent holes continuously attenuate until break from the surrounding plug mass, and a single droplet suspends at the center of the plug configuration. The plug film ring on walls continues deformation until finally breaks into four pieces.

As the plug is relatively long, for example, $l_p = 12$ lu, the rupture pattern turns to O_1 in Fig. 10(b).

Table I summarizes the rupture patterns, O_4 , O_2 , O_1 , and O_0 , in terms of channel thickness, H , and initial plug length, L_p (scaled by Vol/SA). The O_4 -rupture is observed only for short plugs in thick channels; O_2 does not appear in square channels; O_1 and O_0 are possible in channels of any thickness. That is, O_2 , O_1 , and O_0 are available in both thin and moderate channels; all four patterns are possible in thick nonsquare channels; in square channels appear O_4 , O_1 , and O_0 . The thicker the channel is, the more holes the rupture yields. The three critical plug lengths, $L_{c2}(H)$, $L_{c1}(H)$, $L_{c0}(H)$ (scaled by Vol/SA), increasing orderly, are the minimum initial plug

 TABLE I. Rupture patterns of plugs in terms of channel thickness, H , and initial plug length, L_p .

Rupture patterns	Initial plug length, $L_p(L_{c2}(H) < L_{c1}(H) < L_{c0}(H))$			
	Thin channel	Moderate channel		Thick channel
	$H \leq 0.4$	$0.4 < H \leq 0.6$	$0.6 < H < 1.0$	$H = 1.0$
O_4	N/A		$L_p < L_{c2}(H)$	$L_p < L_{c1}(H)$
O_2	$L_p < L_{c1}(H)$		$L_{c2}(H) \leq L_p < L_{c1}(H)$	N/A
O_1		$L_{c1}(H) \leq L_p < L_{c0}(H)$		
O_0		$L_p \geq L_{c0}(H)$		

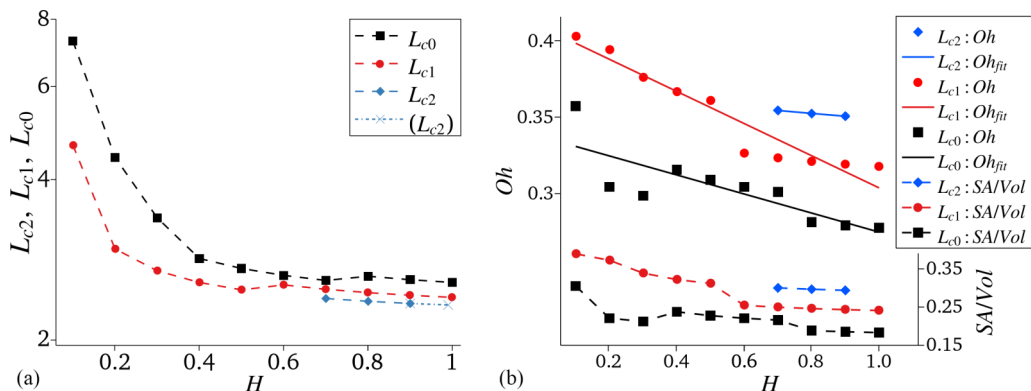


FIG. 11. (a) The critical plug lengths, L_{c2} , L_{c1} , L_{c0} (scaled by Vol/SA), and (b) the Ohnesorge number, Oh , and the surface area-to-volume ratio, SA/Vol, in terms of H . (The dashed lines are for eye-guide. The dash-dot line and cross symbols in panel (a): extrapolated till H is close to 1. The solid lines in panel (b): linear curve-fitting.)

lengths, at which O_2 appears in thick channels, O_1 in channels of any thickness (or O_4 in square channels), and O_0 in channels of any thickness, respectively.

Figure 11(a) further shows the increasing order of the critical plug lengths, L_{c2} , L_{c1} , L_{c0} , at a channel thickness, H . At a given channel thickness, the shorter the plug, the more holes (two or four if applicable) at rupture incipience; the longer the plug, the less possible the rupture. Regarding the effects of channel thickness, more rupture patterns happen in the thicker channels. The plug is more likely to rupture in thin channels, where the critical plug length of no rupture, L_{c0} , is larger than that in moderate and thick channels.

Figure 11(b) gives the relations of the Ohnesorge number, Oh , and the surface area-to-volume ratio of the plug, SA/Vol, with H at L_{c2} , L_{c1} , L_{c0} , respectively. Both Oh and SA/Vol roughly decrease with H increasing. That is, the plug has the larger SA/Vol and Oh in the thinner channel, where the plug is easier to rupture.

IV. DISCUSSION

A. 2D plugs

The contact angle, a measure of wetting ability of a plug, plays dominant roles in the quasiequilibrium plug rupture. The contact angle of $\pi/2$ is critical to tell wetting from nonwetting, and therefore potential rupture of a wetting plug from no rupture of a nonwetting plug in this study (Fig. 5). The rupture pattern indicators, L_{p1} and L_{p0} , quadratically decrease with the contact angle increasing, and both collapse to zero at the contact angle of $\pi/2$. That is, the possibility of plug rupture grows with wetting, which might imply a favorable medical practice that mucus clearance may be improved by increasing wetting of mucus.

Without perturbation embedded in the current ELBM, no droplets of more than two are expected, even though the plug has been as slender as $L_p = 0.004$, for which still one satellite drop appears with rupture [similar to that in Fig. 4(b)]. Such plug rupture of quasiequilibrium basically differs from the breakage of continuous flow into droplet strings, for example, attenuating running water from a faucet, where perturbation-induced instability gets involved. In a wider scope, the plug rupture shares similarity with film rupture, a classic topic in fluid mechanics, which is usually also understood as a result of instability from some disturbance [56–58].

With the assumption of a quasiequilibrium process, the rupture here is triggered by surface tension. A plug deforms its surfaces in a channel for the minimum free-surface energy, but it will have to break its geometry wholeness, i.e., rupture, if its limited volume in one piece fails to maintain



FIG. 12. Deformation and rupture of a spindle plug. ($\chi_\rho = 100.7$, $\gamma_{100} = 0.3348$, and $\theta = 1.20$ rad).

the required surface shapes. It should be pointed out, however, to understand rupture of a liquid droplet or film in reality, besides surface tension and instability as aforementioned, we might need to consider more factors, for example, thermal phenomena of heat transfer and structure of contact surfaces in the micro-/nanoscope [59].

The initial shape of a wetting plug does not influence the effects of surface tension on plug rupture, as shown in Fig. 12, where a spindle plug ruptures like the rectangular one in Figs. 4(a) and 4(d). The self-correction of initial deviations from physics gives a good example of the ELBM's robustness and rationality in multiphase studies.

B. 3D plugs

For plug rupture in a rectangular-cross-sectioned channel in 3D, besides initial plug length, the channel thickness is another impact factor that determines plug deformation and rupture (Fig. 11). Plugs are less likely to rupture in the moderate channel than in the thin. Rupture patterns, however, are somewhat similar, except that films deform more variously on walls of moderate channels than on those of the thin.

Rupture in thick channels shows the most varieties of configurations not only within the channel but also on channel walls (Fig. 9). Plugs in square channels (Fig. 10) rupture similarly as those in the generic thick channels (Fig. 9), but in 90° -rotational symmetry due to the squareness of the channels. A droplet may be left and suspend in the middle of the channel after rupture [Fig. 9(a)], which might be annoying for mucus clearance in large airways. Droplets left after rupture were also observed in plug rupture experiments [60]. Though further study is needed, plug rupture in the nonsquare channels would help with understanding of mucus plug rupture in collapsed lung airways.

The channel thickness-dependence implies the influence of the plug's surface area-to-volume ratio, SA/Vol. The plug in the thinner channel has the larger SA/Vol, i.e., the smaller length dimension characterized by Vol/SA. Plug rupture is the result of the combined effects of the viscous, surface tension, and inertial forces. The viscous force [$\sim \mathcal{O}(\mu ul)$], proportional to Vol/SA, tends to dissipate plug energy as to deform the plug, and thus favors rupture. The inertial force [$\sim \mathcal{O}(u\rho^2 l^2)$], proportional to (Vol/SA)² and maintaining the status quo of the plug, is potentially against such change as deformation and/or rupture. Surface tension has the tendency to minimize the plug surface area, i.e., decreasing SA/Vol, to a minimum Gibbs free energy. Such SA/Vol-reducing efforts for smallest free energy make the plug more likely to deform, even rupture, at the larger SA/Vol. The plug in the thinner channel, often yielding the larger SA/Vol and Oh, thus is easier to rupture. The larger Ohnesorge number in the thinner channel in Fig. 11 justifies the combined effects of the three forces of viscosity, surface tension and inertia. The results imply complexity in mucus clearance that multiple influential factors, for example, mucus plug's properties (e.g., viscosity, surface tension and density), and airway's geometry (e.g., size and shape), should be considered together.

V. CONCLUSIONS

We established an entropic lattice Boltzmann model to study deformation and rupture of plugs, surface tension, and dimensions of plugs and channels in two and three dimensions.

Plug rupture is basically the combined outcome of surface tension, viscous and inertial forces, which may be indicated by the Ohnesorge number, the ratio of the viscous force and the geometric mean of the other two. The chance of plug rupture rises with the Ohnesorge number increasing, i.e., relatively small surface tension, small inertial, and great viscous forces. The Ohnesorge number is correlated positively to the surface area-to-volume ratio of the plug but negatively to channel thickness.

The contact angle, indicating wetting (hydrophilic) or nonwetting (hydrophobic) properties of liquids at solid walls, is a significant factor in plug rupture. The plug is easier to rupture as it is more wetting with the smaller contact angle. A nonwetting plug does not rupture and ends up forming a round droplet in equilibrium.

A (wetting) plug tends to rupture as its initial length is less than a minimum (critical) length, which depends on fluid properties (density ratio, surface tension coefficient, and contact angle), and channel dimensions [channel width and thickness (for 3D only)]. In a 2D channel are observed two patterns of plug rupture, satellite-droplet-rupture (starting from two holes and ending up a droplet suspending in the channel plus films attached to walls) at small initial plug length, and film-rupture (with only one hole and wall-attached films but no suspending droplet) at the large. The minimum plug lengths for the two rupture patterns quadratically decrease with the contact angle increasing, and slightly increase with surface tension.

For 3D rupture, the minimum plug length of no rupture decreases with channel thickness increasing (at given density ratio and surface tension), i.e., more likely for a plug to rupture in the thinner channel. The patterns of rupture incipience in thin ($H \leq 0.4$) and moderate ($0.4 < H \leq 0.6$) channels are similar to those in 2D channels. A new pattern of rupture incipience, four holes, may happen, but in thick channels only ($H > 0.6$) and at relatively small initial plug length. No two-hole rupture appears in square channels due to 90° -rotational symmetry. With the initial plug length increasing, the rupture pattern turns from four-hole (applicable to thick channels only), to two-hole (inapplicable to square channels), then one-hole, and finally no-hole (no rupture), for each pattern of which to happen there exists a minimum initial plug length.

In general, results show great potential of ELBM in the study of multiphase fluid flows. As mucus clearance in lung airways is concerned, we might expect an effective practice through increasing the wetting ability of mucus. Further and full consideration on mucus clearance should include the combined effects of the three forces of viscosity, surface tension and inertia, plus dimensions of both mucus plugs and lung airways. The current finding suggests that mucus clearance be favored as the viscous force is greater than the geometrical mean of the surface tension and inertial forces.

-
- [1] S. A. Bahrani, S. Hamidouche, M. Moazzen, K. Seck, C. Duc, M. Muradoglu, J. B. Grotberg, and F. Romanò, Propagation and rupture of elastoviscoplastic liquid plugs in airway reopening model, *J. Non-Newtonian Fluid Mech.* **300**, 104718 (2022).
 - [2] O. Erken, F. Romanò, J. Grotberg, and M. Muradoglu, Capillary instability of a two-layer annular film: An airway closure model, *J. Fluid Mech.* **934**, A7 (2022).
 - [3] Y. Hu, F. Romanò, and J. B. Grotberg, Effects of surface tension and yield stress on mucus plug rupture: A numerical study, *J. Biomech. Eng.-Trans. ASME* **142**, 061007 (2020).
 - [4] M. Muradoglu, F. Romanò, H. Fujioka, and J. B. Grotberg, Effects of surfactant on propagation and rupture of a liquid plug in a tube, *J. Fluid Mech.* **872**, 407 (2019).
 - [5] J. D. Shemilt, A. Horsley, O. E. Jensen, A. B. Thompson, and C. A. Whitfield, Surface-tension-driven evolution of a viscoplastic liquid coating the interior of a cylindrical tube, *J. Fluid Mech.* **944**, A22 (2022).

- [6] S. Signe Mamba, J. C. Magniez, F. Zoueshtiagh, and M. Baudoin, Dynamics of a liquid plug in a capillary tube under cyclic forcing: Memory effects and airway reopening, *J. Fluid Mech.* **838**, 165 (2018).
- [7] A. G. Ford, X.-Z. Cao, M. J. Papanikolas, T. Kato, R. C. Boucher, M. R. Markovetz, D. B. Hill, R. Freeman, and M. G. Forest, Molecular dynamics simulations to explore the structure and rheological properties of normal and hyperconcentrated airway mucus, *Stud. Appl. Math.* **147**, 1369 (2021).
- [8] F. Romanò, H. Fujioka, M. Muradoglu, and J. B. Grotberg, Liquid plug formation in an airway closure model, *Phys. Rev. Fluids* **4**, 093103 (2019).
- [9] O. Erken, B. Fazla, M. Muradoglu, D. Izbassarov, F. Romanó, and J. B. Grotberg, Effects of elastoviscoplastic properties of mucus on airway closure in healthy and pathological conditions, *Phys. Rev. Fluids* **8**, 053102 (2023).
- [10] A. Galko, S. Gsell, U. D’Ortona, L. Morin, and J. Favier, Pulsated Herschel-Bulkley flows in two-dimensional channels: A model for mucus clearance devices, *Phys. Rev. Fluids* **7**, 053301 (2022).
- [11] D. Hill, B. Button, M. Rubinstein, and R. Boucher, Physiology and pathophysiology of human airway mucus, *Physiol. Rev.* **102**, 1757 (2022).
- [12] F. Romanò, M. Muradoglu, H. Fujioka, and J. B. Grotberg, The effect of viscoelasticity in an airway closure model, *J. Fluid Mech.* **913**, A31 (2021).
- [13] H. Fujioka and J. B. Grotberg, The steady propagation of a surfactant-laden liquid plug in a two-dimensional channel, *Phys. Fluids* **17**, 082102 (2005).
- [14] H. Tavana, P. Zamankhan, P. J. Christensen, J. B. Grotberg, and S. Takayama, Epithelium damage and protection during reopening of occluded airways in a physiologic microfluidic pulmonary airway model, *Biomed. Microdevices* **13**, 731 (2011).
- [15] F. Gibou, R. Fedkiw, and S. Osher, A review of level-set methods and some recent applications, *J. Comput. Phys.* **353**, 82 (2018).
- [16] W. Kim and H. Choi, Immersed boundary methods for fluid-structure interaction: A review, *Int. J. Heat Fluid Flow* **75**, 301 (2019).
- [17] T. Marić, D. B. Kothe, and D. Bothe, Unstructured un-split geometrical volume-of-fluid methods—A review, *J. Comput. Phys.* **420**, 109695 (2020).
- [18] C. K. Aidun and J. R. Clausen, Lattice-Boltzmann method for complex flows, *Annu. Rev. Fluid Mech.* **42**, 439 (2010).
- [19] G. Falcucci, S. Ubertini, D. Chiappini, and S. Succi, Modern lattice Boltzmann methods for multiphase microflows, *IMA J. Appl. Math.* **76**, 712 (2011).
- [20] H. Huang, S. Michael, and X.-Y. Lu, *Multiphase Lattice Boltzmann Methods: Theory and Applications* (John Wiley & Sons, New York, NY, 2015).
- [21] K. J. Petersen and J. R. Brinkerhoff, On the lattice Boltzmann method and its application to turbulent, multiphase flows of various fluids including cryogenics: A review, *Phys. Fluids* **33**, 041302 (2021).
- [22] J. Zhang, Lattice Boltzmann method for microfluidics: Models and applications, *Microfluid. Nanofluid.* **10**, 1 (2011).
- [23] X. Shan and H. Chen, Simulation of nonideal gases and liquid-gas phase transitions by the lattice Boltzmann equation, *Phys. Rev. E* **49**, 2941 (1994).
- [24] Y. Zhao, G. G. Pereira, S. Kuang, and B. Shi, On a modified pseudopotential lattice Boltzmann model for multicomponent flows, *Appl. Math. Lett.* **114**, 106926 (2021).
- [25] X. He, S. Chen, and Z. Raoyang, A lattice Boltzmann scheme for incompressible multiphase flow and its application in simulation of Rayleigh-Taylor instability, *J. Comput. Phys.* **152**, 642 (1999).
- [26] M. R. Swift, E. Orlandini, W. R. Osborn, and J. M. Yeomans, Lattice Boltzmann simulations of liquid-gas and binary fluid systems, *Phys. Rev. E* **54**, 5041 (1996).
- [27] M. R. Swift, W. R. Osborn, and J. M. Yeomans, Lattice Boltzmann Simulation of Nonideal Fluids, *Phys. Rev. Lett.* **75**, 830 (1995).
- [28] Y. Ba, N. Wang, H. Liu, Q. Li, and G. He, Regularized lattice Boltzmann model for immiscible two-phase flows with power-law rheology, *Phys. Rev. E* **97**, 033307 (2018).
- [29] L. Chen, Q. Kang, Y. Mu, Y.-L. He, and W.-Q. Tao, A critical review of the pseudopotential multiphase lattice Boltzmann model: Methods and applications, *Int. J. Heat Mass Transf.* **76**, 210 (2014).

- [30] A. K. Gunstensen, D. H. Rothman, S. Zaleski, and G. Zanetti, Lattice Boltzmann model of immiscible fluids, *Phys. Rev. A* **43**, 4320 (1991).
- [31] P. Lallemand, L.-S. Luo, and Y. Peng, A lattice Boltzmann front-tracking method for interface dynamics with surface tension in two dimensions, *J. Comput. Phys.* **226**, 1367 (2007).
- [32] G. Thömmes, J. Becker, M. Junk, A. K. Vaikuntam, D. Kehrwald, A. Klar, K. Steiner, and A. Wiegmann, A lattice Boltzmann method for immiscible multiphase flow simulations using the level set method, *J. Comput. Phys.* **228**, 1139 (2009).
- [33] M. Geier and A. Pasquali, Fourth order galilean invariance for the lattice Boltzmann method, *Comput. Fluids* **166**, 139 (2018).
- [34] T. Inamuro, N. Konishi, and F. Ogino, A Galilean invariant model of the lattice Boltzmann method for multiphase fluid flows using free-energy approach, *Comput. Phys. Commun.* **129**, 32 (2000).
- [35] P. Lallemand and L.-S. Luo, Theory of the lattice Boltzmann method: Dispersion, dissipation, isotropy, Galilean invariance, and stability, *Phys. Rev. E* **61**, 6546 (2000).
- [36] X. B. Nie, X. Shan, and H. Chen, Galilean invariance of lattice Boltzmann models, *Europhys. Lett.* **81**, 34005 (2008).
- [37] C. Coreixas, G. Wissocq, B. Chopard, and J. Latt, Impact of collision models on the physical properties and the stability of lattice Boltzmann methods, *Philos. Trans. Roy. Soc. A* **378**, 20190397 (2020).
- [38] O. Ilyin, Low dissipative entropic lattice Boltzmann method, *Mathematics* **10**, 3928 (2022).
- [39] R. Machado, On pressure and corner boundary conditions with two lattice Boltzmann construction approaches, *Math. Comput. Simul.* **84**, 26 (2012).
- [40] M. Chavez-Modena, E. Ferrer, and G. Rubio, Improving the stability of multiple-relaxation lattice Boltzmann methods with central moments, *Comput. Fluids* **172**, 397 (2018).
- [41] V. Zecevic, M. P. Kirkpatrick, and S. W. Armfield, Rectangular lattice Boltzmann method using multiple relaxation time collision operator in two and three dimensions, *Comput. Fluids* **202**, 104492 (2020).
- [42] A. Montessori, G. Falcucci, P. Prestininzi, M. La Rocca, and S. Succi, Regularized lattice Bhatnagar-Gross-Krook model for two- and three-dimensional cavity flow simulations, *Phys. Rev. E* **89**, 053317 (2014).
- [43] R. Zhang, X. Shan, and H. Chen, Efficient kinetic method for fluid simulation beyond the Navier-Stokes equation, *Phys. Rev. E* **74**, 046703 (2006).
- [44] A. Jonnalagadda, A. Sharma, and A. Agrawal, Single relaxation time entropic lattice Boltzmann methods: A developer's perspective for stable and accurate simulations, *Comput. Fluids* **215**, 104792 (2021).
- [45] I. V. Karlin, A. N. Gorban, S. Succi, and V. Boffi, Maximum Entropy Principle for Lattice Kinetic Equations, *Phys. Rev. Lett.* **81**, 6 (1998).
- [46] I. V. Karlin, A. Ferrante, and H. C. Öttinger, Perfect entropy functions of the lattice Boltzmann method, *Europhys. Lett.* **47**, 182 (1999).
- [47] A. Mazloomi M, S. S. Chikatamarla, and I. V. Karlin, Entropic Lattice Boltzmann Method for Multiphase Flows, *Phys. Rev. Lett.* **114**, 174502 (2015).
- [48] A. Montessori, P. Prestininzi, M. La Rocca, and S. Succi, Entropic lattice pseudo-potentials for multiphase flow simulations at high Weber and Reynolds numbers, *Phys. Fluids* **29**, 092103 (2017).
- [49] M. E. McCracken and J. Abraham, Multiple-relaxation-time lattice-Boltzmann model for multiphase flow, *Phys. Rev. E* **71**, 036701 (2005).
- [50] A. Kupershtokh, D. Medvedev, and D. Karpov, On equations of state in a lattice Boltzmann method, *Comput. Math. Appl.* **58**, 965 (2009).
- [51] D.-Y. Peng and D. B. Robinson, A new two-constant equation of state, *Ind. Eng. Chem. Fund.* **15**, 59 (1976).
- [52] P. Yuan and L. Schaefer, Equations of state in a lattice Boltzmann model, *Phys. Fluids* **18**, 042101 (2006).
- [53] E. Monaco, G. Brenner, and K. H. Luo, Numerical simulation of the collision of two microdroplets with a pseudopotential multiple-relaxation-time lattice Boltzmann model, *Microfluid. Nanofluid.* **16**, 329 (2014).
- [54] S. Succi, *The Lattice Boltzmann Equation for Complex States of Flowing Matter* (Oxford University Press, Oxford, UK, 2018).

- [55] A. Mazloomi Moqaddam, S. S. Chikatamarla, and I. V. Karlin, Simulation of binary droplet collisions with the entropic lattice Boltzmann method, *Phys. Fluids* **28**, 022106 (2016).
- [56] G. Agbaglah, Breakup of thin liquid sheets through hole-hole and hole-rim merging, *J. Fluid Mech.* **911**, A23 (2021).
- [57] F. E. C. Culick, Comments on a ruptured soap film, *J. Appl. Phys.* **31**, 1128 (1960).
- [58] G. I. Taylor, The dynamics of thin sheets of fluid ii. waves on fluid sheets, *Proc. R. Soc. London A* **253**, 296 (1959).
- [59] D. Lohse and E. Villermaux, Double threshold behavior for breakup of liquid sheets, *Proc. Natl. Acad. Sci. USA* **117**, 18912 (2020).
- [60] Y. Hu, S. Bian, J. Grothberg, M. Filoche, J. White, S. Takayama, and J. B. Grothberg, A microfluidic model to study fluid dynamics of mucus plug rupture in small lung airways, *Biomechanics* **9**, 044119 (2015).